Article

3D Field-Scale Geomechanical Modeling of Potential CO$_2$ Storage Site Smeaheia, Offshore Norway

Md Jamilur Rahman [1,*] , **Manzar Fawad** [1] **and Nazmul Haque Mondol** [1,2]

1   Department of Geosciences, University of Oslo (UiO), 0371 Oslo, Norway; manzar.fawad@geo.uio.no (M.F.); m.n.h.mondol@geo.uio.no (N.H.M.)
2   Norwegian Geotechnical Institute (NGI), 0806 Oslo, Norway
*   Correspondence: m.j.rahman@geo.uio.no; Tel.: +47-41383196

Abstract: Injection-induced rock mechanical failure risks are critical in CO$_2$ sequestration, and thus there is a need to evaluate these occurrences to ensure safe and reliable subsurface storage. A stress–strain-based numerical simulation can reveal the potential mechanical risks of any CO$_2$ sites. This study investigated the hydromechanical effect on geomechanical failure due to injection-induced stress and pore pressure changes in the prospective CO$_2$ storage site Smeaheia, offshore Norway. An inverted-seismic-property-driven 3D field-scale geomechanical model was carried out in the Smeaheia area to evaluate the rock failure and deformation risks in various pressure-build-up scenarios. A one-way coupling between the before- and after-injection pressure scenarios of nine different models has been iterated using the finite element method. The effect of the sensitivity of total pore volume and pore compressibility on rock mechanical deformation is also evaluated. Although various models illustrated comparative variability on failure potential, no model predicted caprock failure or fracture based on the Mohr–Coulomb failure envelope. Moreover, the lateral mechanical failure variation among different locations indicated the possibility to identify a safer injection point with less chances of leakage. In addition, the pore volume and pore compressibility significantly influence the mechanical behavior of the reservoir and caprock rocks. Although this analysis could predict better injection locations based on geomechanical behavior, a fluid simulation model needs to be simulated for assessing lateral and vertical plume migration before making an injection decision.

Keywords: Smeaheia; 3D geomechanical model; caprock; finite element method; tensile failure

1. Introduction

The subsurface state of stress defines the reliability of a field or basin and depends on the structure of the subsurface (geometry of layers, fault location, orientation, etc.), the spatial distribution of rock properties (strength and elastic properties), and the far-field stresses (pore pressure and tectonic stresses) [1]. A geomechanical model is a numerical representation of the state of stress and rock mechanical properties where all the components are included and assessed dynamically. As the geological sequestration of anthropogenic CO$_2$ changes the subsurface state of stress by injecting CO$_2$ into the saline aquifers or depleted reservoirs, a field-scale geomechanical assessment is crucial for safe, reliable, and permanent subsurface CO$_2$ storage. Changes in the state of stress might influence the rocks' (i.e., reservoir, cap, and overburden) mechanical behavior. There might be several potential geomechanical consequences such as top-seal and overburden flexure, reactivation of existing faults, pressure-induced share failure or fracture, formation of new faults, changes in porosity/permeability within the reservoir, etc. [2–8]. Therefore, a thorough geomechanical assessment is critical to evaluate CO$_2$ storage sites.

The studied injection site, the Smeaheia area in the Horda Platform (HP), northern North Sea, is one of the potential subsurface CO$_2$ storage sites. It is bounded by two regional N-S trending faults: the Vette fault in the west and the Øygarden fault complex

in the east (Figure 1a). Two structural closures named Alpha (32/4-1) and Beta (32/2-1) are located in the Smeaheia area, where both structures are three-way closures against the Vette and Øygarden faults, respectively. The area is positioned east of the giant Troll east gas field and has the same reservoir–caprock pairs. The main reservoirs consist of Upper to Middle Jurassic Sognefjord, Fensfjord, and Krossfjord formation sandstones with good to moderate reservoir quality [9–11] and were deposited in a shallow coastal marine environment, interfingering with Heather Formation shales (Figure 1b). The primary caprock of the studied area also consists of Upper Jurassic shale formations such as organic-rich Draupne and Heather formation shales. Both formations are deposited in an open marine environment with restricted bottom circulation and often anaerobic conditions [12]. A thick westward-dipping overburden rock package is also present, mainly consisting of fine- to coarse-grained siliciclastic with occasional carbonate-rich deposits [13].

Effective vertical stress-dependent mechanical compaction deformed the rocks by frictional slippage, rotation, sliding, and reorientation of grains [14,15], which can be obtained by subtracting pore pressure from the total vertical stress. The total vertical stress is carried out by the grain framework (solid phase) and the pore pressure (fluid phase). Therefore, the effective vertical stress is only transmitted through the grain contacts and deforms the rock. Injecting CO_2 into the subsurface would increase the reservoir pore pressure, which influences the normal stresses but not the shear stress because fluid is unable to transfer shear properties. Therefore, the effective normal stress is directly related to the total normal stress and pore pressure, which changes the state of stress and, hence, mechanical properties [16]. Although the pore pressure changes are confined within the reservoir due to the tensor characteristic of the stress, the induced stresses can transfer and deform the overburden and underburden rock layers. To predict the injection-related changes in CO_2 storage, a 3D geomechanical model with spatially gridded overburden and underburden layers is essential.

The tectonic stress regime and failure mechanisms also play a vital role during rock deformation. The magnitude and order of the principal stresses vary from basin to basin with a defined stress regime within that specific area. Three different stress regimes, such as extensional (normal faulting), compressional (reverse faulting), and strike-slip (strike-slip or wrench faulting), are considered, which is called Andersonic fault classification ([17,18]; Figure 2). The failure plane varies based on the stress regime condition. Moreover, the pore pressure and stress coupling significantly change in different stress regimes. The Mohr diagram shift due to pore pressure changes is affected substantially by the stress regime (Figure 2).

A hydromechanical (HM) coupling can describe the geomechanical deformation due to stress and pore pressure changes [19,20]. A fluid-saturated porous rock can be deformed by changing the external load (i.e., overburden stress) or the internal pore fluid pressure change (i.e., injection or production). This poromechanics behavior of a fluid-saturated rock can be defined by introducing a numerical simulated geomechanical modeling approach where the mechanical and hydraulic processes affect each other through changing the material properties. However, building a geomechanical model requires the integration of various parameters. For instance, the caprock and overburden section are mostly ignored during the acquisition of relevant databases compared to the reservoir interval and use simple assumptions in the modeling workflow [21–30]. Irrespective of the data limitation, the effectiveness of 3D field-scale geomechanical modeling in rock deformation and failure has been proven and published by several authors for CO_2 injection and gas storage projects worldwide [21,22,24–29]. However, the conventional 1D well property-point-interpolation method and a simple assumption in the missing interval (mainly caprock and overburden sections) have been considered in most of the models. The interpolation method increases the spatial properties' distribution uncertainty significantly if limited wells are present. Moreover, a simple assumption is missing the anisotropic behavior of the properties. Seismic-data-driven models can resolve the spatial anisotropic issue; however, to date, they have only focused on the reservoir and caprock intervals [3,31]. Considering these

issues, Rahman et al. [32] proposed the seismic-inverted-property-driven 3D field-scale geomechanical model workflow, where an integrated approach has been introduced. This study is the continuation of that modeling work, in which the field-scale geomechanical failure risks for the Smeaheia area in offshore Norway have been assessed to evaluate the mechanical behavior of rocks during CO_2 injection into the sandstone reservoirs of Sognefjord, Fensfjord, and Krossfjord formations.
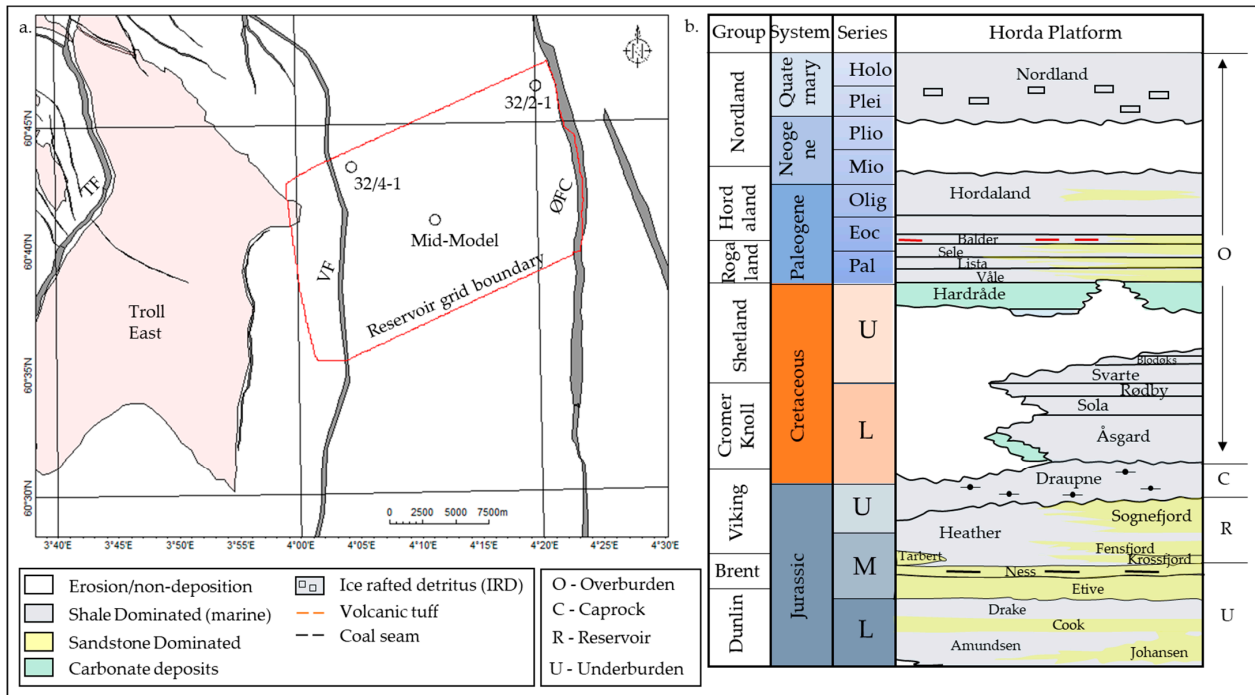
Figure 1. The map of the study area represents the model boundary (red polygon) and the bounding faults (ØFC—Øygarden fault complex; VF—Vette fault) with the studied locations such as 32/4-1, 32/2-1, and Mid-Model (**a**). The area is located east of the Troll east field, which is bounded by VF and TF (Tusse fault). A few minor faults (gray lines) are also illustrated. (**b**) A generalized stratigraphic succession of Horda Platform from Lower Jurassic to Quaternary is presented where the overburden, caprock, reservoir, and underburden sections are also marked (modified after [32]).

Seismic-property-driven field-scale geomechanical modeling was analyzed to investigate the CO_2-injection-induced failure potential and rock deformation in the Smeaheia area. The main objective was to evaluate the sensitivity of rock compressibility and the pore volume effect on the reservoir and caprock failure potential in Alpha (32/4-1), Beta (32/2-1), and Mid-Model (i:j—50:50) locations (Figure 1a). Moreover, the total vertical displacement of the reservoir and caprocks was also estimated and analyzed. Finally, a comparative assessment between the different injection points as well as worst-case and best-case injection scenarios in the Smeaheia site area is discussed. The credibility and practicality of the seismic-property-based modeling approach was tested by Rahman et al. [32]; hence, it is directly used in this research.

4 of 21
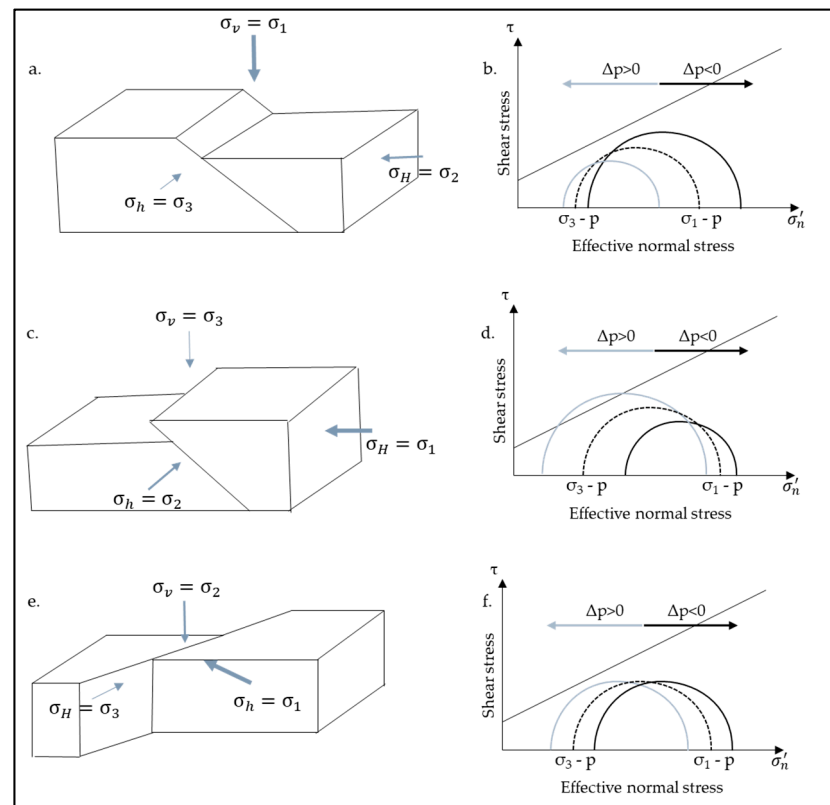
Figure 2. Shows the magnitude and order of principal stresses and the corresponding Mohr–Coulomb diagram effect of pore pressure changes on extensional stress (**a**,**b**), compressional stress (**c**,**d**), and strike-slip (**e**,**f**) regimes (modified after Altmann, [18]).

2. Model Setup

A detailed description of the model-building processes was presented in Rahman et al. [32]; the model with spatially distributed overburden properties was adapted for this study. The overburden rock properties have considerable variation, which influences the mechanical rock failure potential; hence, the model considered both spatial and temporal variations of overburden properties. The model properties (overburden, cap, reservoir, and underburden rocks) were estimated from the prestacked simultaneous inversion using a 3D seismic survey named GN1101 [33]. The properties of 3D cubes allowed us to have better vertical and horizontal control of rock properties than the conventional wireline log-based property-interpolation techniques. However, we needed a proper calibration of these property cubes before using them in the reservoir models. Fourteen (14) seismic interpreted time surfaces (i.e., top Nordland GP., top Rogaland GP., top Lista Fm., top Shetland GP., top Svarte Fm., top Rødby Fm., top Asgård Fm., top Draupne Fm., top Sognefjord Fm., top Heather Fm., top Fensfjord Fm., top Krossfjord Fm., top Dunlin GP. and top Statfjord GP.) were used to build the structural grid. Faults were considered during interpretation but not included in the grid as a separate element. The 3D properties were later distributed within the reservoir grid using the seismic resampling function in the Petrel-2019 geometrical modeling module. However, each of reservoir grids had a unique value estimated from the seismic cube. The average properties of each layer have been given in Table 1 for better clarity. The reservoir model with properties was then converted from time domain to depth domain using the velocity model constructed from the average velocity cube, which was estimated from the 3D stacking velocity. To mitigate the boundary effects and buckling artifacts over the zone of interest (i.e., reservoir model area), the reservoir grid was expanded laterally and vertically to a certain extent. The hydrostatic gradient was used for the initial pore pressure during the boundary condition, while the lithostatic gradient was considered for the vertical stress profile. A normal faulting stress regime was assigned to the study

area. [34–37]. The minimum horizontal stress gradient used was 0.1245 MPa/m, which was estimated from the X-LOT database from the study area [24]. Moreover, the maximum horizontal stress was assumed to be 10% higher than the minimum horizontal stress. In addition, the horizontal stress azimuth was used as 103^0 based on the seismicity database near the Troll field area [34]. The overall workflow for seismic properties based on one-way coupling is illustrated in Figure 3. The model used finite element method-based numerical simulation to evaluate the injection-induced geomechanical risks.

Table 1. Average properties of the model grids show the variations among different model zones.

Zones	Density (g/cm^3)	E (GPa)	PR	FA (^{0})	UCS (Mpa)
Nordaland Gp.	2.14	0.4	0.45	24.51	5.03
Rogaland Gp.	2.18	1.23	0.39	26.96	9.41
Lista Fm.	2.31	2.57	0.35	26.19	16.46
Shetland Gp.	2.24	1.44	0.39	26.19	10.35
Svarte Fm.	2.27	2.03	0.36	26.46	14.01
Rødby Fm.	2.27	1.59	0.38	25.93	11.01
Asgård Fm.	2.25	1.44	0.39	25.20	10.04
Draupne Fm.	2.31	2.15	0.37	25.43	13.96
Sognefjord Fm.	2.23	2.63	0.34	27.97	16.80
Heather Fm.	2.25	2.95	0.33	27.97	17.99
Fensfjord Fm.	2.28	3.46	0.32	28.22	21.03
Krossfjord Fm.	2.34	3.95	0.31	27.44	23.40
Dunlin Gp.	2.44	4.48	0.3	26.78	24.95

The fluid simulation model was out of the scope of this study; however, the pressure build-up due to 50 years of CO_2 injection was directly adapted from the study performed by Gassnova [38]. Based on the Gassnova [38] model, nine different scenarios were simulated and analyzed (Table 2). The reservoir simulation model was built based on the geological structures with an injection rate of 3.2 million tonnes per year for a period of 50 years. The average porosity within the reservoir interval is 0.26, while the permeability is 690 mD (milidarcy), and the K_v/K_h ratio is equal to 0.1. Moreover, the solubility of CO_2 in water was not considered because a study on the sensitivity of solubility revealed a minor effect on the fluid simulation model [38]. Although the amount of total injected CO_2 was the same within the studied model, based on the different pore volumes and pore compressibility, the pressure increase within the reservoir significantly varied (Table 2). Gassnova [38] was defined the total pore volume based on the different criteria. For instance, the low case volume (51 GSm^3) was estimated based on the boundary to the south as defined by the data available within the Øygarden–Vette fault block, while the southern limit of the sandstones defined the base volume (160 GSm^3). The next western fault block (Vette–Tusse) was also considered for the two high cases, High1 (297 GSm^3) and High2 (418 GSm^3), where the High1 was considered up to the southern limit of the Troll east field, and High2 included all the pore volumes within these two fault blocks. Moreover, the pore volume (rock) compressibility in the Smeaheia area was not defined because of the lack of laboratory experiments. Therefore, Gassnova [38] tried three different models based on the pore compressibility database from SINTEF. The reference case value (4.0×10^{-5} bar^{-1}) was adapted from the Johansen study (Aurora) with a good match in the Smeaheia study (i.e., according to Hall's correlation), while one optimistic (1.6×10^{-4} bar^{-1}) and one pessimistic (1.6×10^{-6} bar^{-1}) case were also simulated. Out of these ten (10) models, nine pressure-build-up-at-the-well-location scenarios were adopted in this study except High2. Although injection-induced pore pressure increases varied spatially (decreases away from the well), we considered a constant reservoir pore pressure increase during geomechanical simulation due to model limitation.
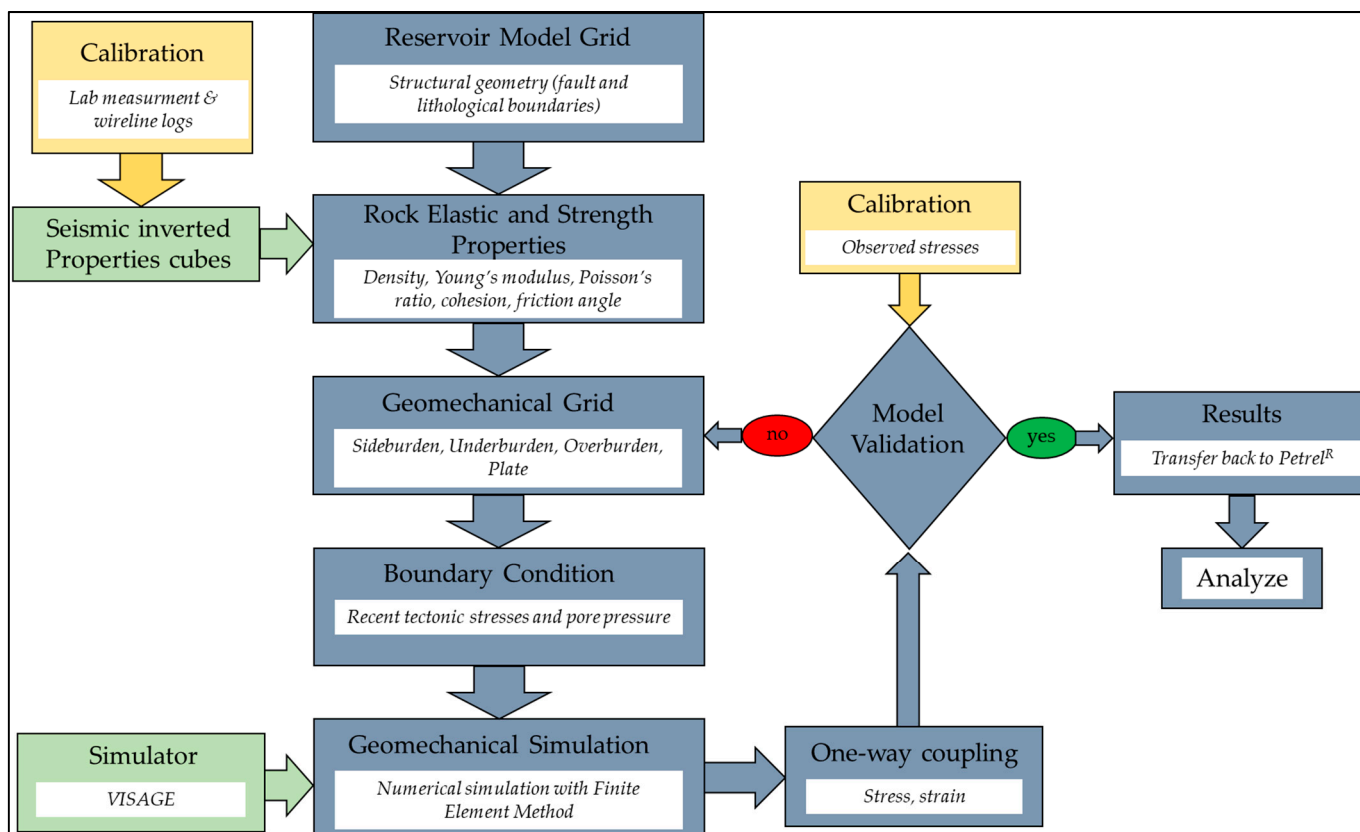
Figure 3. The workflow illustrated the different components of one-way coupling geomechanical model to evaluate the pressure-induced stress and strain change of the studied rocks (adapted from Rahman et al. [32]).

Out of these nine models, three cases were selected for detail analysis where the worst-case (orange) scenario is presented by the 'Pessimistic-Low' scenario, the base case (gray) was combined by the base total pore volume and reference rock compressibility, and the best case (green) was defined by high pore volume with optimistic compressibility (Table 2). The geomechanical failure of these three models (i.e., worst, base, and best cases) are presented in the Results section for comparative analysis. Moreover, three locations, namely Alpha (32/4-1), Beta (32/2-1), and the middle of the model (Mid-Model), were considered for mechanical assessment to find a better location for the optimum injection point (Figure 1a).

Table 2. Pressure increase from hydrostatic in well location after 50 years of injection of 3.2 million tonnes per year (adapted from [38]). The studied worst (orange), base (gray), and best (green) cases are highlighted by different colors.

Rock Compressibility	Total Pore Volume		
	Low	**Base**	**High**
Pessimistic	1.94	1.31	1.19
Reference	1.58	1.20	1.12
Optimistic	1.31	1.12	1.07

The pressure build-up (times) is relative to the initial hydrostatic pressure.

3. Pore Pressure and Effective Stress

Effective stress depends on the in situ stresses and pore pressure. The CO_2-injection-induced pore pressure changes change the effective stresses within the reservoirs, which influence the reservoir and the overburden rocks due to the tensor behavior of the stress.

This study used the hydrostatic pore pressure gradient as the initial reservoir pressure (Figure 4a). The in situ pore pressure decreases from west to east due to the structural dipping (reservoirs dipping towards the west). Moreover, the hanging wall side of the Vette fault (VF) shows comparatively high pore pressure because of depth. However, the Troll east gas field is located within this fault block (Tusse–Vette fault block) and has been in production for several years from the same reservoirs, so one can expect a depleted pore pressure. However, the previous analyses [35,36,39] indicated sealed VF in the study area, so we assumed a hydrostatic gradient in the VF footwall block. Moreover, this study focused on the Smeaheia fault block; hence, it did not adjust the depleted pore pressure on the west side of the VF. Therefore, the hanging wall side (west of the Vette Fault) was not included in any analysis but was retained as the grid considered the complete area of the studied 3D cube (GN1101).
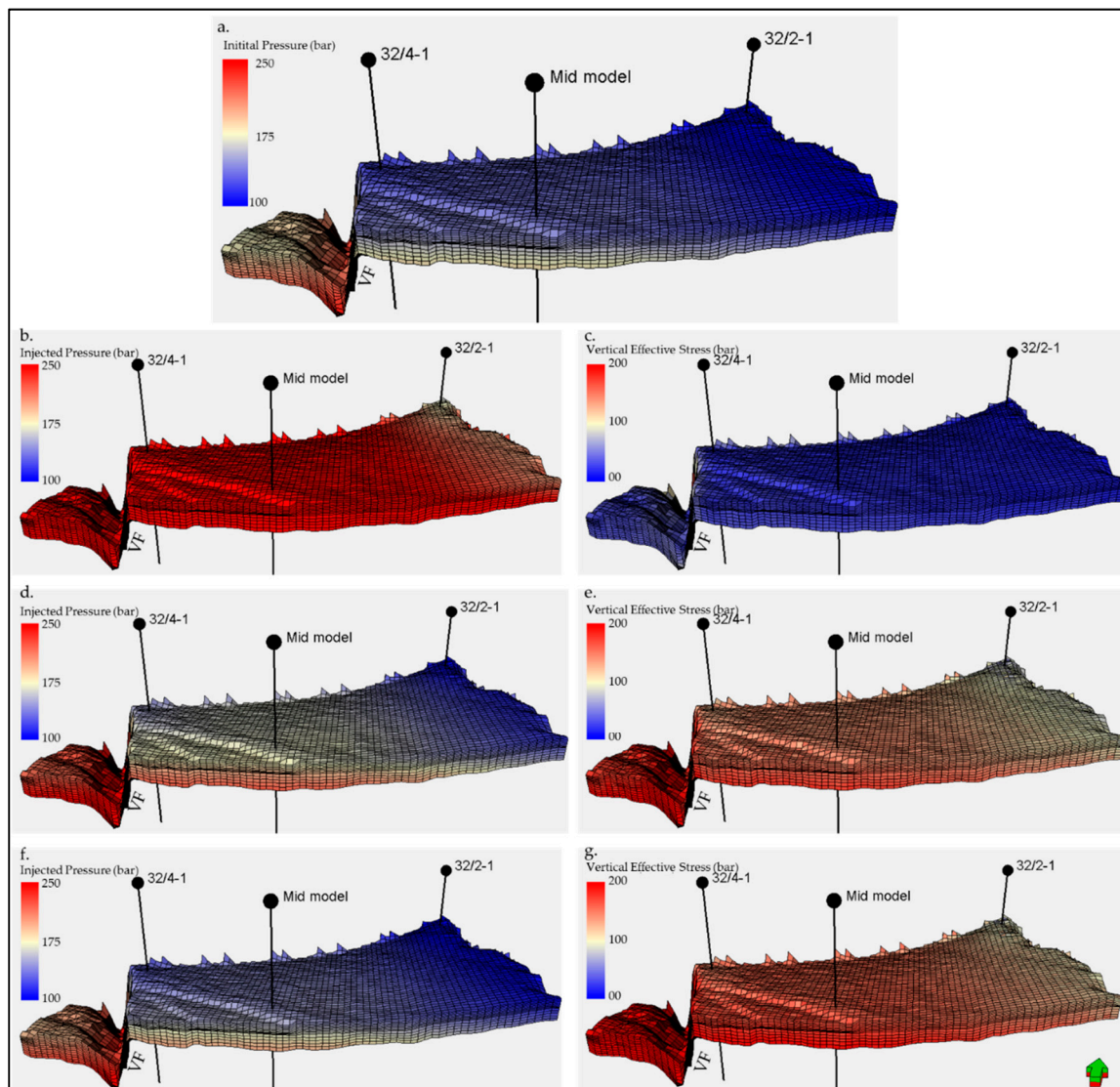
Figure 4. 3D illustration of reservoir grids shows the initial hydrostatic pore pressure (**a**) after-injection pressure and corresponding vertical effective stress in the worst-case model (**b**,**c**), the base-case model (**d**,**e**), and the best-case model (**f**,**g**), respectively. The locations and Vette fault (VF) are shown for reference. Moreover, the green arrow indicated the north direction of the model. Additionally, note that the color scales demonstrate differences between the after-injection pressure and effective vertical stresses.

The CO_2-injection-induced reservoir pressure increase in worst-, base-, and best-case models is illustrated in Figure 4b,d,f, where the worst-case scenario represents a significantly high reservoir pressure increase (~72 bar) compared to base- (~15 bar) and best-case (~6 bar) models. The corresponding vertical effective stresses are also demonstrated in Figure 4c,e,g. The highest reservoir pressure increase model (i.e., worst-case) showed the lowest vertical effective stress and vice versa. The worst case indicated an effective vertical stress of 96 bar, while the base and best cases showed average stresses of 152 and 161 bar, respectively.

4. Results

4.1. Reservoir and Caprock Assessment

The potential geomechanical risks such as failure and deformation were assessed for different rock compressibilities and pore volume scenarios. Four different vertical layers within the studied reservoir (Top Sognefjord and Fensfjord) and caprock (Top and base caprock) were analyzed.

4.1.1. Failure Potential in Different Locations

- Alpha location (well 32/4-1)

Based on the Mohr–Coulomb failure criteria, the model grid penetrated by the well 32/4-1 was evaluated for potential injection-induced failure. All the models showed a similar trend with various intensities; hence, three (i.e., worst-, base-, and best-case models) out of nine models' results are presented here. The potential failure of these models is illustrated in Figure 5. Based on the rock strength and stress-state condition, no caprock failure or fractures were observed in any of the models (Figure 5a,d,g). However, the mobilized shear stress/strength significantly increased at the base of the caprock, which represents the Heather Formation shale (Figure 5b,e,h). The Mohr circles were closer to the Coulomb failure envelope at the base (Heather) compared to the top caprock (Draupne).

Moreover, after 50 years of CO_2 injection, the shear stress/strength increase was negligible within the caprock except for the Heather Formation in the worst-case model, where the Mohr circle shifted to the left, close to the tensile failure line. In the other two models, the caprock Mohr circle was juxtaposed in before- and after-injection scenarios. This indicates a minimal CO_2-injection-induced effect on caprock failure.

On the contrary, the injection-induced reservoir pressure change considerably increased the possibility of tensile fractures within the reservoir (Figure 5c,d,f). There was no fracture observed in the in situ stress-state condition based on the Coulomb failure criteria. However, the worst-case model illustrated significant tensile fracture risks in after-injection scenarios, which decreased in base- and best-case models.

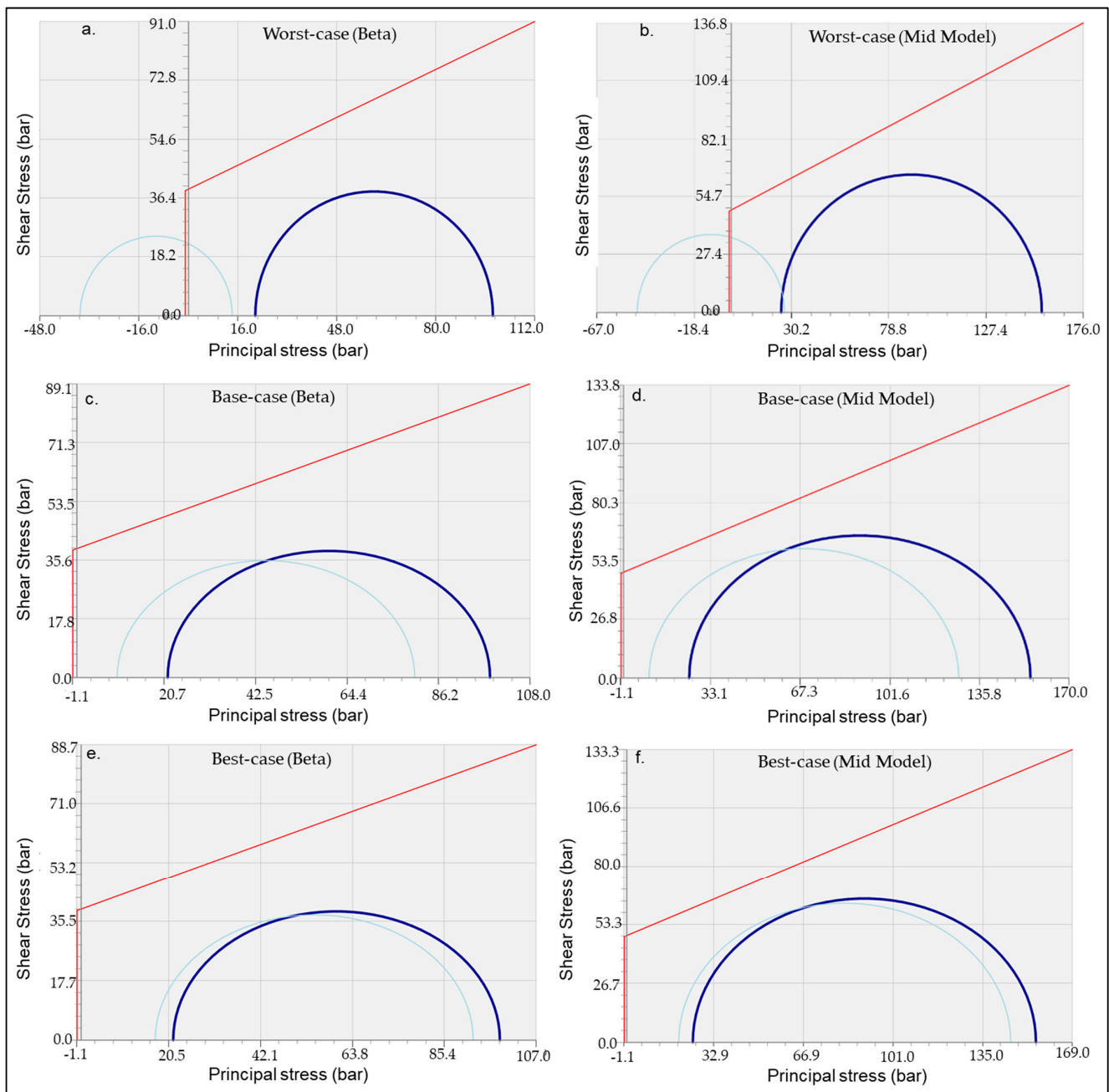- Beta (well 32/2-1) and Mid-Model locations

The Beta location (32/2-1) is structurally shallower compared to Alpha (32/4-1), while the Mid-Model location is deeper than Alpha. For instance, the top reservoir TVD at Beta is 889 m, while the Mid-Model top reservoir depth is 1359 m compared to the top reservoir of Alpha, which is 1250 m. Therefore, lower in situ stresses and initial pore pressure was expected in the Beta location, and higher value were expected in the Mid-Model, considering the same gradient was used in all the models. Moreover, as the injection-induced reservoir pressure change was directly estimated from the initial pore pressure, the pore pressure change also varied spatially (Figure 4). Furthermore, the elastic properties differed both laterally and vertically, which might have had an influence on the numerical simulations.
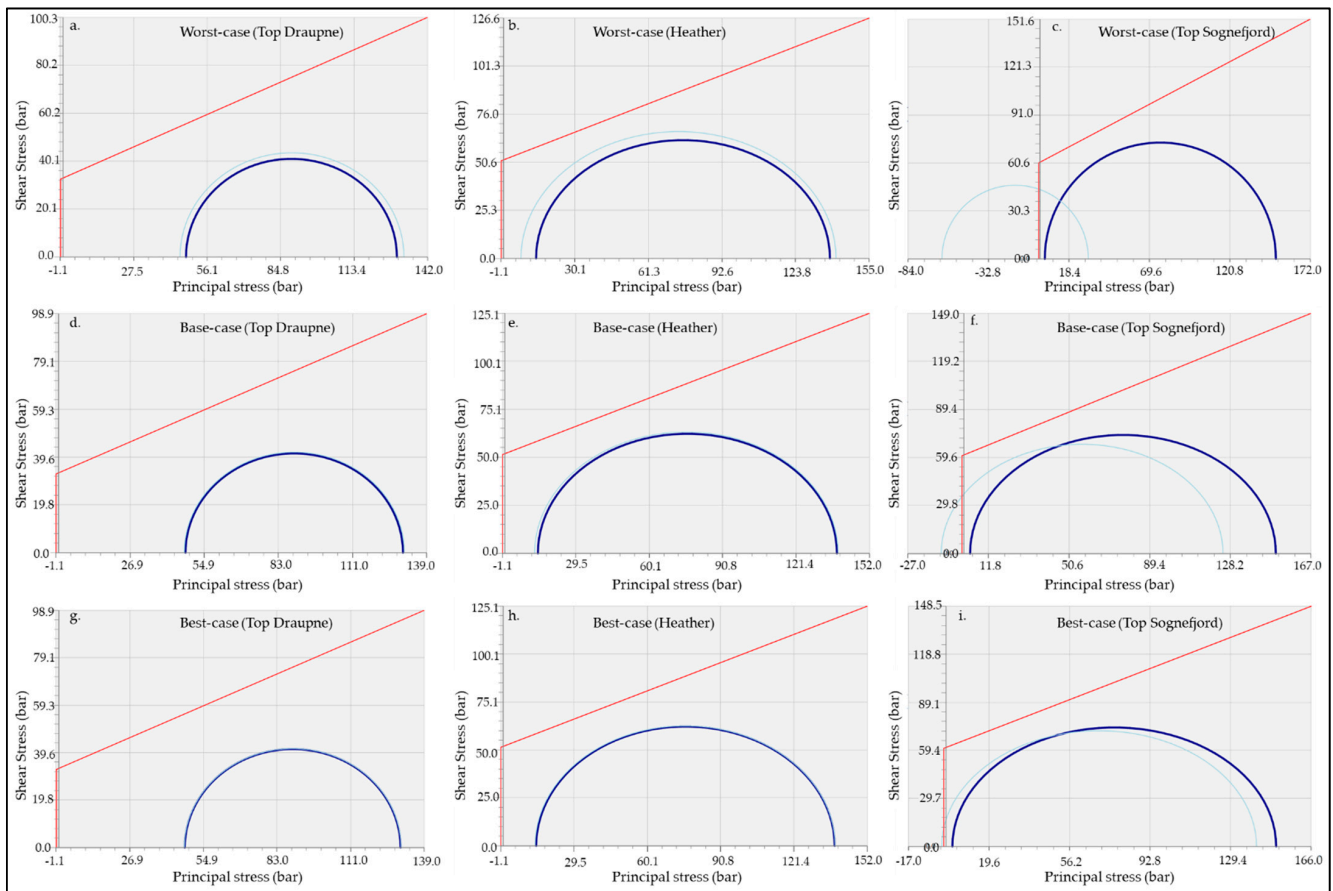
Figure 5. The Mohr–Coulomb failure envelope in Alpha location illustrated the failure potential before- and after-injection periods of top caprock layer (Draupne), base caprock layer (Heather) and top reservoir (Sognefjord) for worst-case model (**a**–**c**), base-case model (**d**–**f**), and best-case model (**g**–**i**), respectively. The dark blue represents the in situ stress state, while the light-blue curve indicates after-injection scenario.

Similar to the Alpha location, there was no caprock failure or fractures observed in either the Beta or Mid-Model locations. However, the shear strength was comparatively high in the Beta structure in contrast with the Mid-Model location. The Mohr–Coulomb failure of the reservoir rock significantly differed in Beta and Mid-Model locations compared to the Alpha location. Although the worst-case models had a tensile failure risk, such as in the Alpha location, the base- and best-case models did not demonstrate any tensile failure (Figure 6). Moreover, based on the tensile failure cut-off (1 bar), the in situ stress-state condition, the failure risk was significantly lower in both Beta and Mid-Model locations than in the Alpha structure. In addition, irrespective of in situ stresses and pore pressure variation between Beta and Mid-Model locations, the reservoir rock strength illustrated a similar trend (i.e., tensile failure in the worst case and no failure in base and best cases), though the Mid-Model case showed slightly lower strength.

Figure 6. The Mohr–Coulomb failure envelopes of the top reservoir (Sognefjord) are illustrated, along with the failure potential before and after injection periods in Beta (32/2-1) and Mid-Model locations for the worst case (**a**,**b**), base case (**c**,**d**), and best case (**e**,**f**), respectively. The dark blue represents the in situ stress state, while the light-blue curve indicates after-injection scenario.

4.2. Effect of Pore-Volume-Induced Pressure Build-Up

The effect of pore volume sensitivity on rock deformation and failure was analyzed by comparing the three pore volume models (i.e., low, base, and high) in a reference case for rock compressibility (Table 2). The vertical rock displacement of the top Draupne and top Sognefjord formations is illustrated in Figure 8. The same color scale was used for all the model cases for a better visual comparison. It is evident that the pore volume change significantly influenced vertical rock displacement. The low pore volume model estimated a maximum displacement of 74 cm, while the high-pore-volume case indicated only a 15 cm maximum uplift. The intermediate base-case model showed a 26 cm uplift.

Comparing the same models in the Mohr–Coulomb failure envelope, the shear stress/strength decreased with increasing pore volume (Figure 9). Although the pore pressure change influenced rock failure or fracture, the changes were minimal considering the studied failure envelope. Therefore, no caprock failure was observed in any case. On the contrary, injection-induced pressure change shifted the Mohr circle in the left direction with tensile failure considering the tensile cut-off of 1 bar. Irrespective of total-pore-volume-induced pressure build-up, after-injection tensile failure within the reservoir was observed in all three cases. However, the strain rate decreased with increasing pore volume. The above Mohr–Coulomb failure analysis was based on the Alpha location. However, interpretation changes in different studied locations (i.e., Beta and Mid-Model) followed a similar trend as described above in location-based comparative analysis.

4.3. Effect of Rock-Compressibility-Induced Pressure Build-Up

The pore compressibility sensitivity was also evaluated by analyzing the pessimistic, reference, and optimistic rock compressibility models, where base case pore volume was used for all three models (Table 2). Similar to the pore volume study, the same color scale was used for visual comparison to show the vertical deformation (Figure 10). The vertical displacement of the caprock and reservoir decreased with increasing pore compressibility values (i.e., optimistic case). However, the maximum uplift difference was not as significant as the pore volume effect, but considerably high, as the pessimistic model estimated a 40 cm uplift compared to 15 cm in the optimistic case. The reference model's maximum upliftment was 26 cm.

Moreover, the Mohr–Coulomb failure envelope revealed that the rock shear stress/strength decreased with increasing pore compressibility; however, the changes were negligible (Figure 11). There was no caprock failure observed, while reservoir tensile failure was determined to potentially occur after injection-induced pressure changes.

4.3.1. Rock Deformation

The vertical rock deformations of top Draupne, top Sognefjord, and top Fensfjord formations are illustrated in Figure 7. The different color scales were used for different models because of the significant differences in the total vertical deformation. The positive deformation indicates upliftment, while the negative value represents subsidence. The studied models indicated overall upliftment due to CO_2-injection-caused pressure changes in the study area. The upliftment between the formation followed a similar pattern in all three models, where the Draupne and Sognefjord formations were uplifted significantly higher compared to the Fensfjord Formation. Lateral upliftment variation was also observed, but the intensity was minimal. However, a significant difference was estimated when comparing the vertical upliftment among the models (i.e., worst, base, and best cases). As expected, high upliftment was observed in the worst-case scenario with the maximum value of 120 cm, while maximum upliftment in the base case was 26 cm and 9 cm in the best-case model.
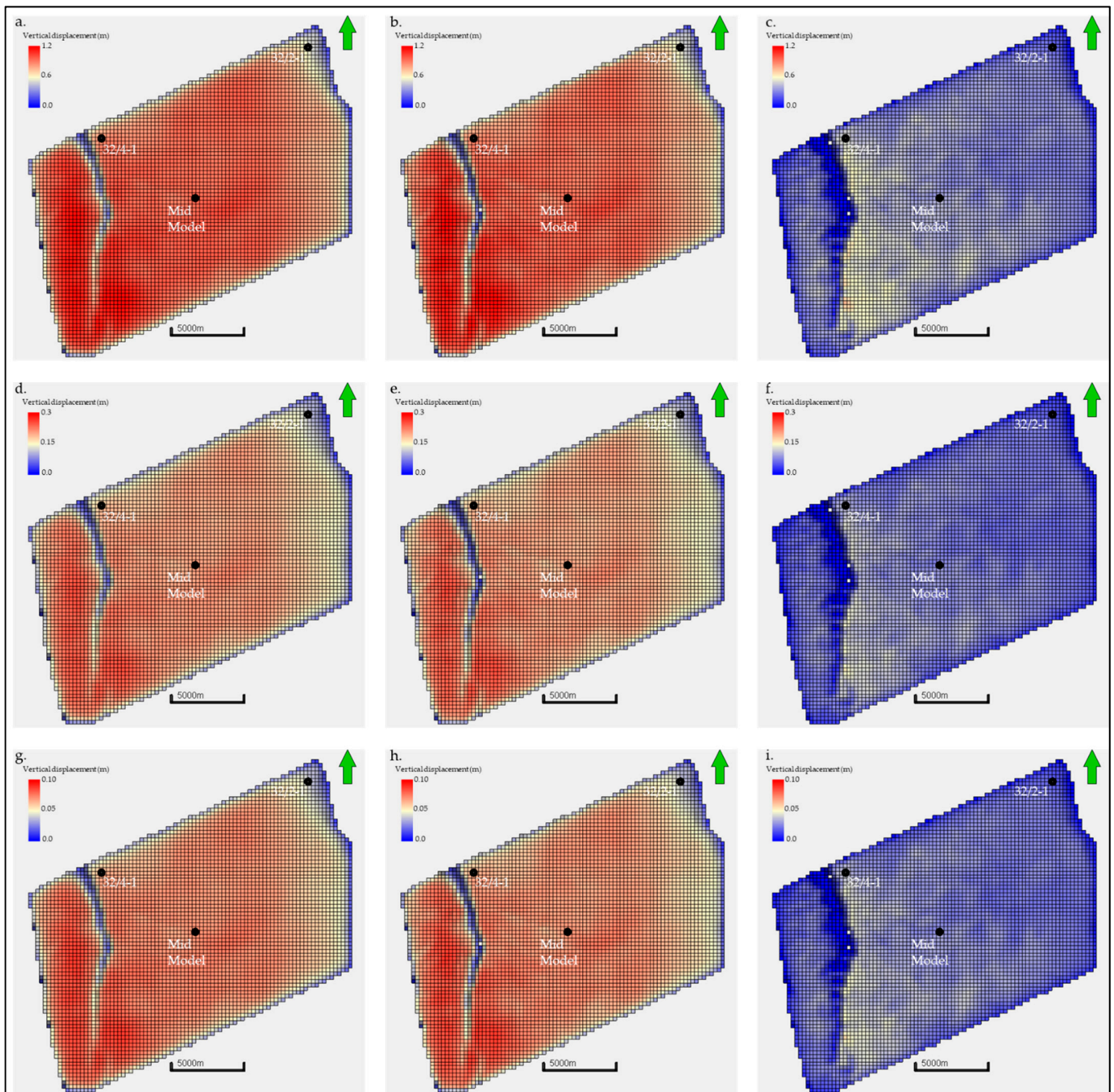
Figure 7. Estimated vertical displacements of the top Draupne, top Sognefjord, and top Fensfjord after injection period show the upliftment for the worst-case model (**a–c**), base-case model (**d–f**), and best-case model (**g–i**), respectively. Note that the color bar varied significantly among models. The Alpha, Beta, and Mid-Model locations are also indicated on the maps for reference. Moreover, the green arrow indicated the north direction of the model.
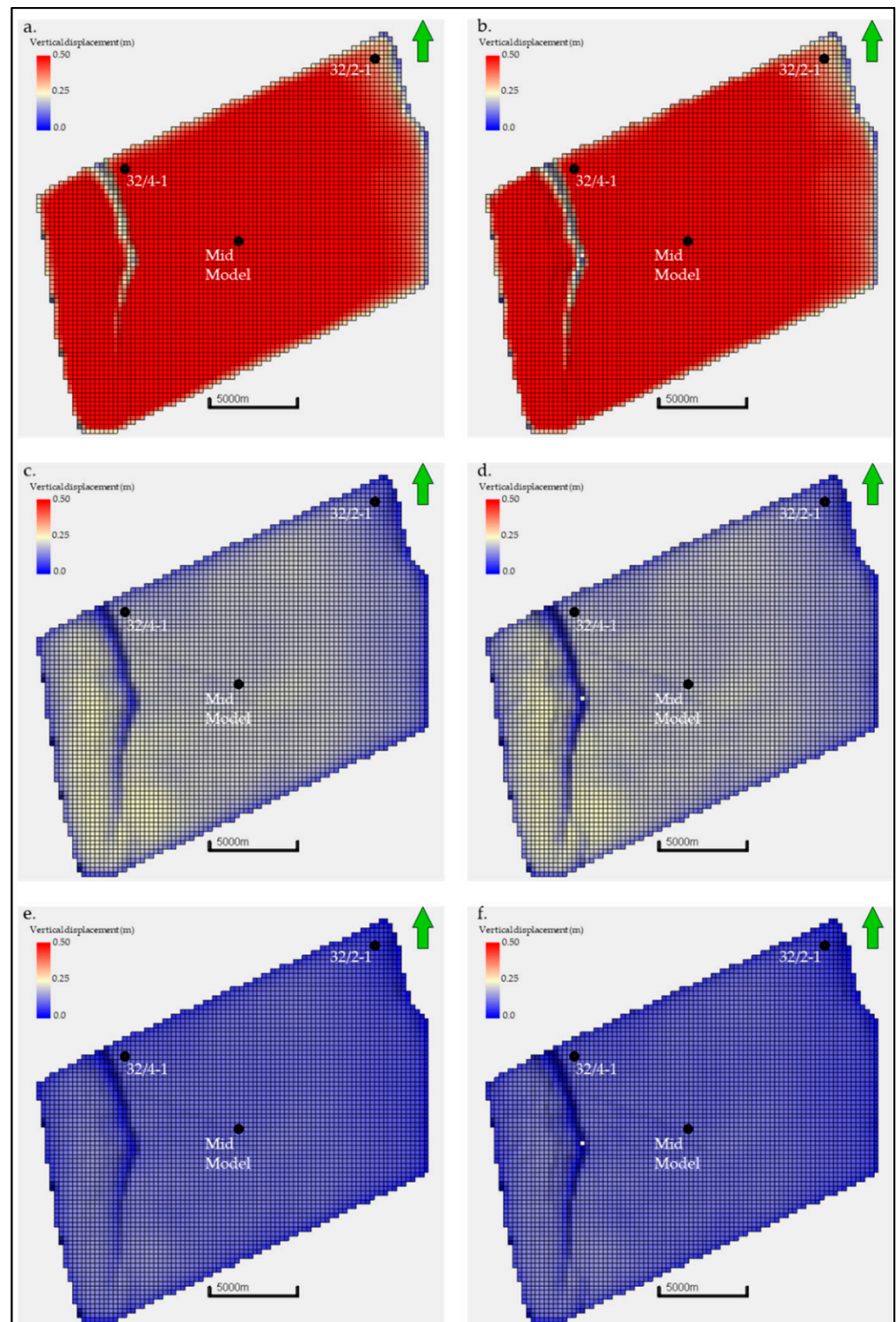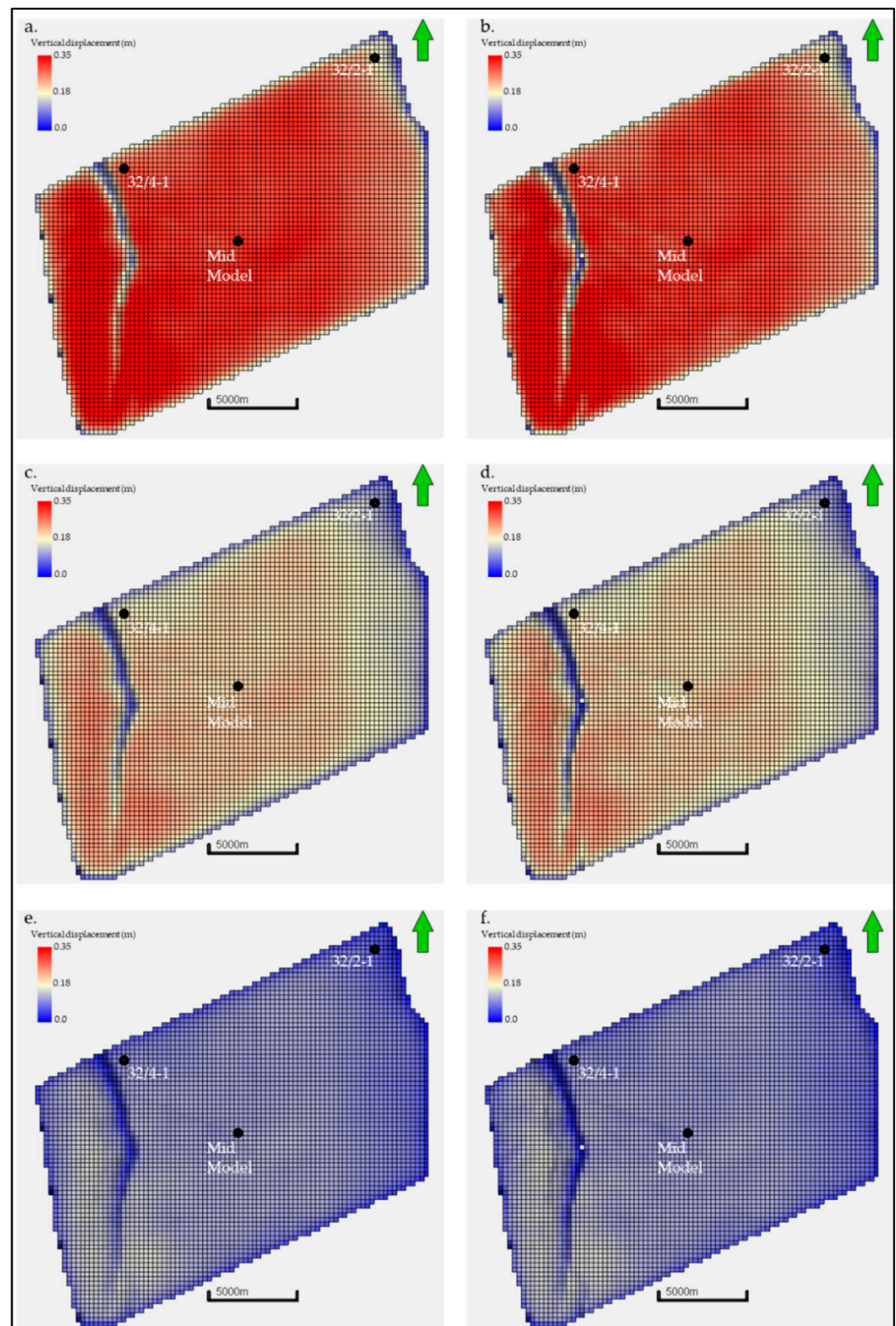
Figure 8. A comparison of vertical displacement of the top Draupne and top Sognefjord after injection period shows the upliftment for model RL (**a**,**b**), model RB (**c**,**d**), and model RH (**e**,**f**), respectively. The Alpha, Beta, and Mid-Model locations are indicated on the maps for reference. Moreover, the green arrow indicated the north direction of the model.
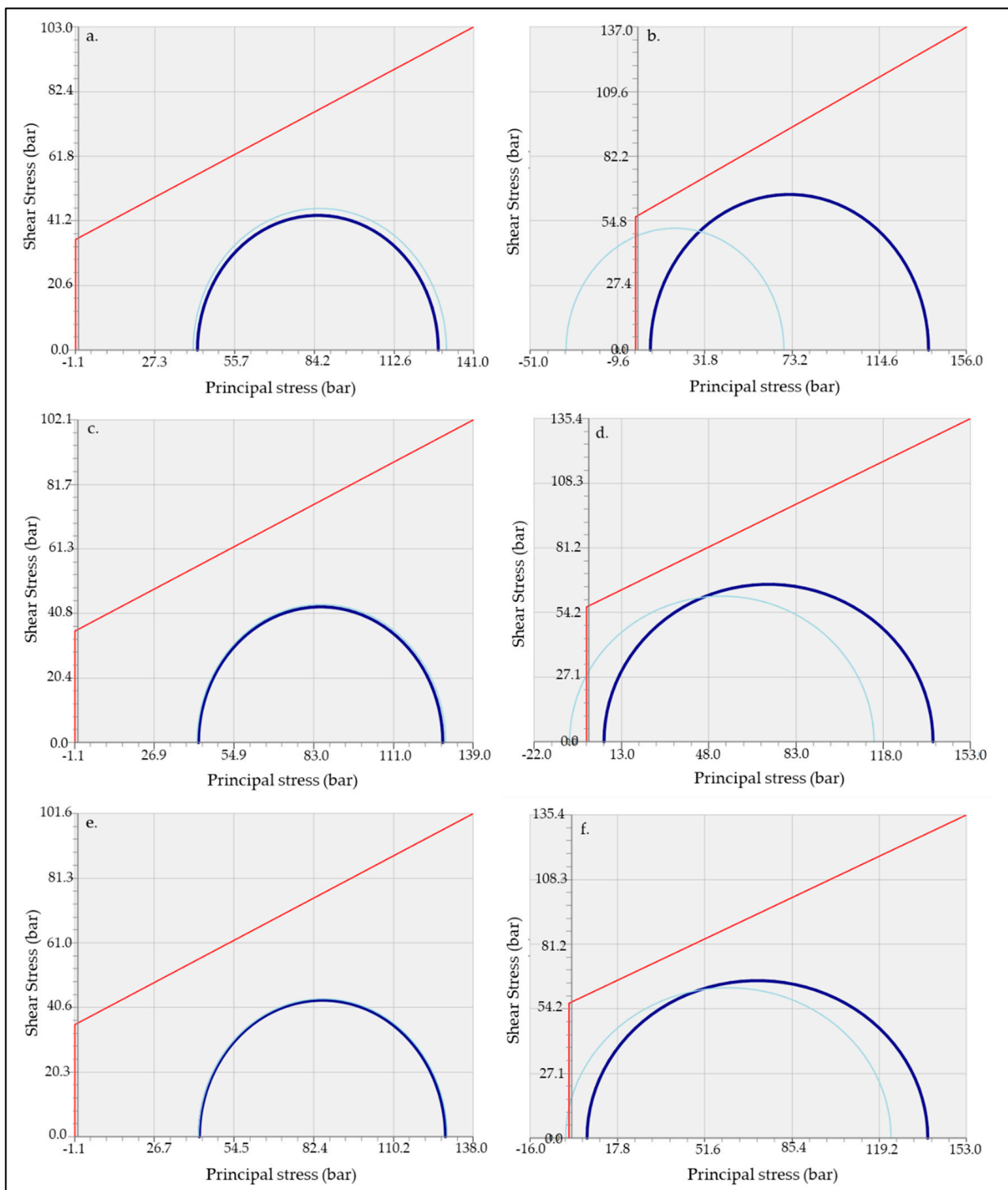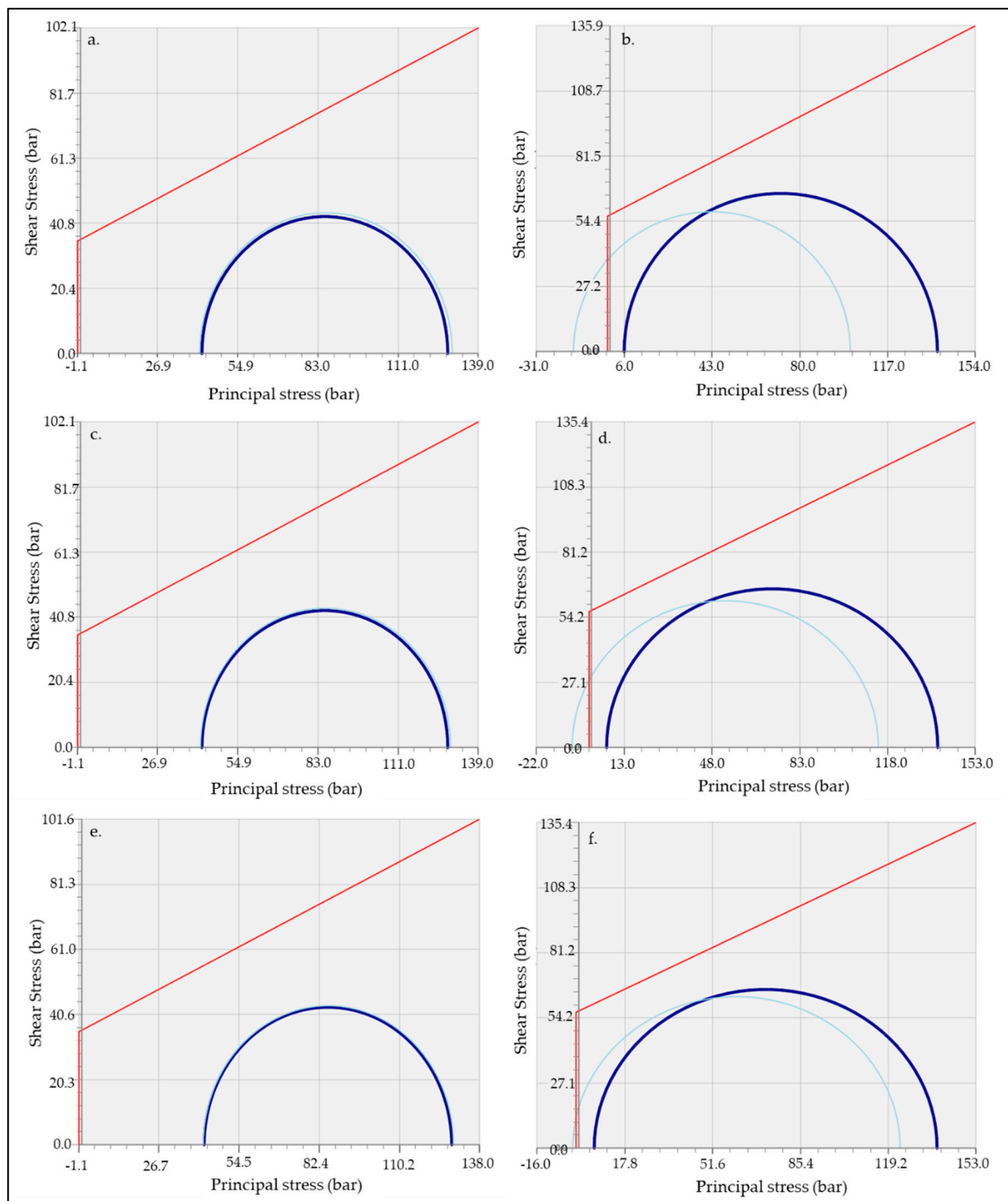
Figure 9. The Mohr–Coulomb failure envelope of top Draupne and top Sognefjord layers in Alpha location illustrated the failure potential of model RL (**a,b**), model RB (**c,d**), and model RH (**e,f**), respectively. Note that the dark blue represents the in situ stress state, while the light-blue curve indicates the post-injection scenario.

Figure 10. A comparison of vertical displacement of the top Draupne and top Sognefjord formations after injection period show the upliftment for model PB (**a**,**b**), model RB (**c**,**d**), and model OB (**e**,**f**), respectively. The Alpha, Beta, and Mid-Model locations are marked on the maps for reference. Moreover, the green arrow indicated the north direction of the model.

Figure 11. The Mohr–Coulomb failure envelope of top Draupne and top Sognefjord layers in Alpha location illustrated the failure potential of the models PB (**a,b**), RB (**c,d**), and OB (**e,f**), respectively. Note that the dark blue represents the in situ stress state, while the light-blue curve indicates post-injection scenario.

5. Discussions

Although there are many uncertainties about the magnitude and order of principal stresses, this study attempted to evaluate the mechanical rock failure and deformation in the Smeaheia area using the available database. However, although the principal stresses significantly influenced the overall field-scale mechanical risks, there was no failure or fracture risk observed within the caprock and reservoir under the initial stress condition. When the injection-induced reservoir pressure increases were introduced within the models, a significant variation was observed among studied model scenarios (i.e., worst, base, and

best cases) and among the various model locations (i.e., Alpha, Beta, and Mid-Model). The differences observed within the various cases were constrained by the pore pressure build-up within the reservoir because the same elastic properties' geomechanical grid had been used for all the models. However, the variation in Alpha, Beta, and Mid-Model locations within the same model illustrated the spatial variation in the seismic-driven elastic properties. This explains the lower failure risk in the Mid-Model location compared to the Alpha location, though the Mid-Model location is structurally deeper. In the Beta location, these could be a combination of low initial stresses and elastic properties as the Beta location is structurally shallower than both Alpha and Mid-Model locations. Mechanical properties such as cohesion varied among the studied locations. For instance, the Alpha location had a 52-bar cohesion within the top Sognefjord layer compared with 40 and 48 bar in Beta and Mid-Model locations, respectively. Therefore, the Coulomb failure envelope changes various shear failures within the locations. Moreover, due to the difference in effective stresses, the Mohr circle position relative to tensile failure cut-off in in situ and after-injection scenarios were varied and influenced the tensile failure risks.

Although the rock failure risks decreased from the worst-case to best-case model, no caprock failure or fracture risks were observed based on the Mohr–Coulomb failure envelope in any case. However, the base caprock layer, equivalent to the Heather Formation shale, poses higher failure risks than the organic-rich upper Draupne caprock shale (Figures 5 and 6). The Heather Formation shale is more brittle than the Draupne shale [40], which explains the higher mechanical failure risk in the base caprock layer. Moreover, the base layer might have more influence due to the reservoir interval below.

The possibility of tensile fracturing within the reservoir in the worst-case scenario after injection was observed in all three locations (i.e., Alpha, Beta, and Mid-Model). However, in base- and best-case models, the reservoir fracture might have only occured in the Alpha location, while the Beta and Mid-Model locations did not have any potential failure risks. The worst-case model represents a closed aquifer (i.e., confined low pore volume) system, which significantly influences the storage efficiency. However, reservoirs commonly have an open system at their margins with lateral and vertical single-phase flow, allowing waters to escape without any detrimental effect on the storage integrity [41]. This indicates that the worst-case scenario is a hypothetical case and does not exist. Nevertheless, we must keep in mind that all the tensile failure risk assessments illustrated in this study are based on the tensile stress cut-off of 1 bar. There was no sensitivity analysis performed in this research; hence, the tensile failure results might vary depending on the tensile stress cut-off value.

The total pore volume and pore compressibility significantly influenced the pressure build-up within the reservoir interval, considering the same volume of CO_2 injected into the aquifer (Table 2). This study reveals the influence on rock deformation and failure of these different pressure build-up scenario models. As we used the same geomechanical grid for all the models, the rock deformation and failure variations observed were due to the pressure difference related to the pore volume and compressibility of the study area. The total pore volume and compressibility significantly influenced the geomechanical behavior of the studied rocks. The maximum vertical upliftment in the low-pore-volume scenario was considerably high, even using the reference pore compressibility value (Figure 12). However, the confined low pore volume is not common in nature [41]. Moreover, the influence of pore compressibility was also high but not significant, like pore volume (Figure 12). Pore compressibility is an important factor and depends on both rock and pore fluid compressibilities. Therefore, this is a complex property and depends on a combination of parameters such as mineralogy, porosity, type of fluid, etc. However, due to the importance of rock compressibility in geomechanical behavior revealed in this study, further investigation is needed, such as laboratory experiments on the well 32/4-1 (Alpha) to reduce the pore volume compressibility uncertainty.
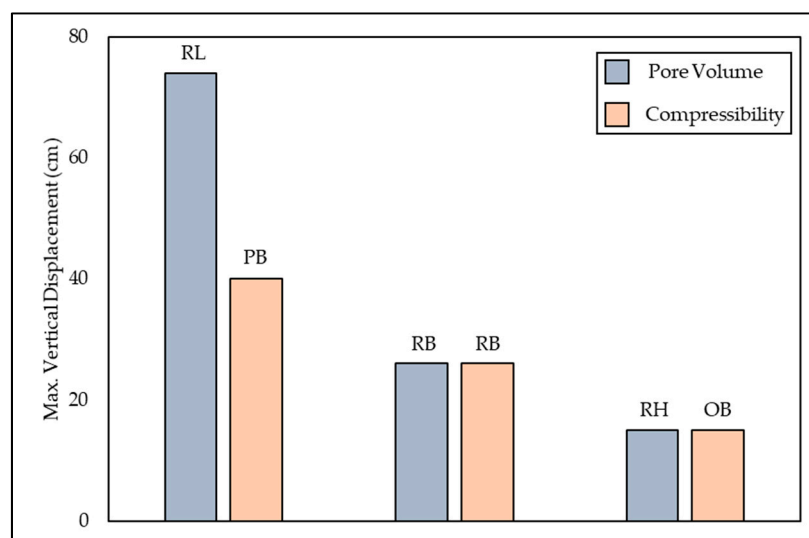
Figure 12. The bar chart illustrates the maximum vertical displacement estimated for different pressure build-up scenarios in various total pore volume and pore compressibility models.

Implication for Geological Storage of CO$_2$

One of the crucial parameters in subsurface CO$_2$ storage is the evaluation of the safe volume of injected CO$_2$. The safe volume of injection-induced pressure build-up describes the amount of CO$_2$ injection before any leakage happens. Moreover, the optimal injectivity (injection rate) played a vital role in a safe CO$_2$ storage project. Estimation of optimal capacity and injectivity of any CO$_2$ injection site is one of the criteria in storage site characterization. A fluid simulation model, which was out of the scope of this work, can assist the studied geomechanical model by providing different pressure changes scenarios as an input. However, the studied scenarios can also reveal the acceptable amount of pressure build-up before any leakage happens. The base-case model we analyzed had a 25-bar reservoir pressure increase. According to Gassnova [38], this is the acceptable amount of pressure build-up in the Smeaheia injection site compared to the base case. The pressure build-up in the worst- and best-case models were 117 bar and 9 bar, respectively. Although Gassnova [38] suggested the base-case model is geomechanically not safe, the caprock failure risk in this study indicated no failure. However, the Vette Fault (for the Alpha structure) and the Øygarden Fault (for the Beta structure) sealing potentials were not investigated here, which may also be critical to assess the overall top seal integrity. The results from this study indicate the practicality of the proposed numerical simulation workflow to evaluate the geomechanical risks in any CO$_2$ injection site.

The CO$_2$ injection point in any CCS project is also essential. The spatial variation of rock failure risks in the same model indicates the importance of having a potentially better location for injection. The failure risk assessment shows that the Beta and Mid-Model locations are safe compared to the Alpha structure. However, considering the Øygarden fault failure risk not addressed in this study, the better location would be the Mid-Model case (i:j—50:50). Nevertheless, the lateral and vertical plume migration and their effects must be evaluated using a fluid simulation model.

Moreover, the fluid flow model needs to be integrated into the modeling workflow because the fluid flow model depicts the actual CO$_2$-injection-induced pressure changes within the reservoir. The pore pressure change varied laterally and vertically based on pore connectivity, injection interval, and locations. Using a constant pressure increase gradient within the whole reservoir (this study) limits the sensitivity analysis to estimate any injection site's optimum capacity and injectivity rate. Nevertheless, this is a future opportunity where fluid flow integrated geomechanical modeling will be executed.

6. Conclusions

The key findings from this study are stated below:

- The pore volume and pore compressibility significantly influenced the mechanical rock failure and deformation. The low pore volume with reference compressibility was estimated at ~74 cm vertical upliftfield on the reservoir–caprock interval, while the pessimistic compressibility model has a base pore volume calculated ~40 cm uplift. Irrespective of considerable vertical upliftment, no caprock failure was observed in any models. However, although there was no reservoir rock failure in in situ stress-state conditions, tensile failure occurred after injection-induced pressure change scenarios.
- The Mohr–Coulomb failure risks varied within the studied locations. Based on the assessment, the Alpha structure indicated low mobilized shear stress/strength compared to the Beta and Mid-Model locations. However, a fluid simulation model should be implemented to evaluate the plume migration for building confidence.

Assuming the base-case as the real injection scenario, the caprock might act as an effective top seal. However, the fault sealing analysis should be carried out before any injection decision.

References

1. Al-Zubaidi, N.S.; Al-Neeamy, A.K. 3D mechanical earth model for Zubair oilfield in southern Iraq. *J. Pet. Explor. Prod. Technol.* **2020**, *10*, 1729–1741. [CrossRef]
2. Hawkes, C.D.; McLellan, P.J.; Bachu, S. Geomechanical factors affecting geological storage of CO_2 in depleted oil and gas reservoirs. In Proceedings of the Canadian International Petroleum Conference, Calgary, AB, Canada, 8 June 2004.
3. Herwanger, J.; Koutsabeloulis, N. *Seismic Geomechanics. How to Build Calibrate Geomech Model Using 3D 4D Seism Data*; EAGE: Kuala Lumpur, Malaysia, 2011.
4. Rutqvist, J.; Birkholzer, J.; Cappa, F.; Tsang, C.-F. Estimating maximum sustainable injection pressure during geological sequestration of CO_2 using coupled fluid flow and geomechanical fault-slip analysis. *Energy Convers. Manag.* **2007**, *48*, 1798–1807. [CrossRef]
5. Rutqvist, J.; Birkholzer, J.T.; Tsang, C.-F. Coupled reservoir–geomechanical analysis of the potential for tensile and shear failure associated with CO_2 injection in multilayered reservoir–caprock systems. *Int. J. Rock Mech. Min. Sci.* **2008**, *45*, 132–143. [CrossRef]
6. Soltanzadeh, H.; Hawkes, C.D. Semi-analytical models for stress change and fault reactivation induced by reservoir production and injection. *J. Pet. Sci. Eng.* **2008**, *60*, 71–85. [CrossRef]
7. Streit, J.E.; Hillis, R.R. Estimating fault stability and sustainable fluid pressures for underground storage of CO_2 in porous rock. *Energy* **2004**, *29*, 1445–1456. [CrossRef]
8. Ganguli, S.S.; Sen, S. Investigation of present-day in-situ stresses and pore pressure in the south Cambay Basin, western India: Implications for drilling, reservoir development and fault reactivation. *Mar. Pet. Geol.* **2020**, *118*, 104422. [CrossRef]

9. Fawad, M.; Rahman, M.D.J.; Mondol, N.H. Seismic reservoir characterization of potential CO_2 storage reservoir sandstones in Smeaheia area, Northern North Sea. *J. Pet. Sci. Eng.* **2021**, *205*, 108812. [CrossRef]
10. Dreyer, T.; Whitaker, M.; Dexter, J.; Flesche, H.; Larsen, E. From spit system to tide-dominated delta: Integrated reservoir model of the Upper Jurassic Sognefjord Formation on the Troll West Field. *Geol. Soc. Lond. Pet. Geol. Conf. Ser.* **2005**, *6*, 423–448. [CrossRef]
11. Holgate, N.E.; Jackson, C.A.L.; Hampson, G.J.; Dreyer, T. Seismic stratigraphic analysis of the Middle Jurassic Krossfjord and Fensfjord formations, Troll oil and gas field, northern North Sea. *Mar. Pet. Geol.* **2015**, *68*, 352–380. [CrossRef]
12. NPD. NPD FactPages. 2021. Available online: https://npdfactpages.npd.no/factpages/Default.aspx?culture=en (accessed on 20 December 2021).
13. Faleide, J.I.; Bjørlykke, K.; Gabrielsen, R.H. Geology of the Norwegian Continental Shelf. In *Petroleum Geoscience*; Springer: Berlin/Heidelberg, Germany, 2015; pp. 603–637.
14. Chuhan, F.A.; Kjeldstad, A.; Bjørlykke, K.; Høeg, K. Porosity loss in sand by grain crushing—Experimental evidence and relevance to reservoir quality. *Mar. Pet. Geol.* **2002**, *19*, 39–53. [CrossRef]
15. Bjørlykke, K. Compaction of Sedimentary Rocks: Shales, Sandstones and Carbonates. In *Petroleum Geoscience*; Springer: Berlin/Heidelberg, Germany, 2015; pp. 351–360.
16. Terzaghi, K. *Theoretical Soil Mechanics*; John Wiley & Sons: New York, NY, USA, 1943; pp. 11–15.
17. Anderson, E.M. The dynamics of faulting. *Trans. Edinburgh Geol. Soc.* **1905**, *8*, 387–402. [CrossRef]
18. Altmann, J.B. Poroelastic Effects in Reservoir Modelling. Ph.D. Dissertation, Karlsruher Institut für Technologie, Karlsruhe, Germany, 2010.
19. Kümpel, H.J. *Theory of Linear Poroelasticity—With Applications to Geomechanics and Hydrogeology*; Wang, H.F., Ed.; Princeton University Press: Princeton, NJ, USA, 2000; p. 287.
20. Rutqvist, J.; Stephansson, O. The role of hydromechanical coupling in fractured rock engineering. *HydroGeol. J.* **2003**, *11*, 7–40. [CrossRef]
21. Fischer, K.; Henk, A. A workflow for building and calibrating 3-D geomechanical models &ndash a case study for a gas reservoir in the North German Basin. *Solid Earth* **2013**, *4*, 347–355.
22. Fokker, P.A.; Orlic, B.; Van der Meer, L.G.H.; Geel, C.R. Geomechanical modeling of surface uplift around well KB-502 at the In Salah CO_2 storage site. In Proceedings of the 73rd EAGE Conference and Exhibition Incorporating SPE EUROPEC 2011, Vienna, Austria, 23–27 May 2011.
23. Grollimund, B.; Zoback, M.D. Impact of glacially induced stress changes on fault-seal integrity offshore Norway. *Am. Assoc. Pet. Geol. Bull.* **2003**, *87*, 493–506. [CrossRef]
24. Mandal, P.P.; Essa, I.; Saha, S.; Rezaee, R. *Multi-Purpose Utility of Constructing 3D Static Geomechanical Model in the Ichthys Field, Browse Basin*; AEGC: Brisbane, Australia, 2021.
25. Newell, P.; Yoon, H.; Martinez, M.J.; Bishop, J.E.; Bryant, S.L. Investigation of the influence of geomechanical and hydrogeological properties on surface uplift at In Salah. *J. Pet. Sci. Eng.* **2017**, *155*, 34–45. [CrossRef]
26. Olden, P.; Jin, M.; Pickup, G.; Mackay, E.; Hamilton, S.; Somerville, J.; Todd, A. Geomechanical modelling of CO_2 geological storage with the use of site specific rock mechanics laboratory data. *Pet. Geosci.* **2014**, *20*, 323–337. [CrossRef]
27. Ouellet, A.; Bérard, T.; Desroches, J.; Frykman, P.; Welsh, P.; Minton, J.; Pamukcu, Y.; Hurter, S.; Schmidt-Hattenberger, C. Reservoir geomechanics for assessing containment in CO_2 storage: A case study at Ketzin, Germany. *Energy Procedia* **2011**, *4*, 3298–3305. [CrossRef]
28. Tenthorey, E.; Vidal-Gilbert, S.; Backe, G.; Puspitasari, R.; Pallikathekathil, Z.J.; Maney, B.; Dewhurst, D. Modelling the geomechanics of gas storage: A case study from the Iona gas field, Australia. *Int. J. Greenh. Gas Control* **2013**, *13*, 138–148. [CrossRef]
29. Vidal-Gilbert, S.; Tenthorey, E.; Dewhurst, D.; Ennis-King, J.; Van Ruth, P.; Hillis, R. Geomechanical analysis of the Naylor Field, Otway Basin, Australia: Implications for CO_2 injection and storage. *Int. J. Greenh. Gas Control* **2010**, *4*, 827–839. [CrossRef]
30. Ganguli, S.S.; Vedanti, N.; Akervoll, I.; Dimri, V.P. Assessing the feasibility of CO_2-enhanced oil recovery and storage in mature oil field: A case study from Cambay Basin. *J. Geol. Soc. India* **2016**, *88*, 273–280. [CrossRef]
31. Sengupta, M.; Dai, J.; Volterrani, S.; Dutta, N.; Rao, N.S.; Al-Qadeeri, B.; Kidambi, V.K. Building a Seismic-Driven 3D Geomechanical Model in a Deep Carbonate Reservoir. In *SEG Technical Program Expanded Abstracts 2011*; Society of Exploration Geophysicists: Tulsa, OK, USA, 2011; pp. 2069–2073.
32. Rahman, M.J.; Fawad, M.; Choi, J.C.; Mondol, N.H. Effect of overburden spatial variability on field-scale geomechanical modeling of potential CO_2 storage site Smeaheia, offshore Norway. *J. Nat. Gas Sci. Eng.* **2022**, *99*, 104453. [CrossRef]
33. Fawad, M.; Rahman, M.J.; Mondol, N.H. Seismic-derived geomechanical properties of potential CO_2 storage reservoir and cap rock in Smeaheia area, northern North Sea. *Lead. Edge* **2021**, *40*, 254–260. [CrossRef]
34. Heidbach, O.; Rajabi, M.; Cui, X.; Fuchs, K.; Müller, B.; Reinecker, J.; Reiter, K.; Tingay, M.; Wenzel, F.; Xie, F.; et al. The World Stress Map database release 2016: Crustal stress pattern across scales. *Tectonophysics* **2018**, *744*, 484–498. [CrossRef]
35. Rahman, M.J.; Choi, J.C.; Fawad, M.; Mondol, N.H. Probabilistic analysis of Vette fault stability in potential CO_2 storage site Smeaheia, offshore Norway. *Int. J. Greenh. Gas Control* **2021**, *108*, 103315. [CrossRef]
36. Skurtveit, E.; Choi, J.C.; Osmond, J.; Mulrooney, M.; Braathen, A. 3D fault integrity screening for smeaheia CO_2 injection site. In Proceedings of the 14th Greenhouse Gas Control Technologies Conference, Melbourne, Australia, 21–26 October 2018; pp. 21–26.

37. Thompson, N.; Andrews, J.S.; Wu, L.; Meneguolo, R. Characterization of the in-situ stress on the Horda platform–A study from the Northern Lights Eos well. *Int. J. Greenh. Gas Control* **2022**, *114*, 103580. [CrossRef]
38. Gassnova. Troll Kystnær Subsurface Status Report. Report no. TL02-ROS-Z-RA-005, Rev. 3. 2012. Available online: https://ccsnorway.com/app/uploads/sites/6/2019/09/tl02-ros-z-ra-0005-troll-kystnaer-subsurface-status-report-rev03.pdf (accessed on 2 January 2022).
39. Michie, E.A.H.; Mulrooney, M.J.; Braathen, A. Fault interpretation uncertainties using seismic data, and the effects on fault seal analysis: A case study from the Horda Platform, with implications for CO_2 storage. *Solid Earth* **2021**, *12*, 1259–1286. [CrossRef]
40. Rahman, M.J.; Fawad, M.; Mondol, N.H. Organic-rich shale caprock properties of potential CO_2 storage sites in the northern North Sea, offshore Norway. *Mar. Pet. Geol.* **2020**, *122*, 104665. [CrossRef]
41. Chadwick, A.; Smith, D.; Hodrien, C.; Hovorka, S.; Mackay, E.; Mathias, S.; Lovell, B.; Kalaydjian, F.; Sweeney, G.; Benson, S.; et al. The realities of storing carbon dioxide—A response to CO_2 storage capacity issues raised by Ehlig-Economides & Economides. *Nat. Preced* **2010**. [CrossRef]